

Top-of-atmosphere radiation budget of convective core/stratiform rain and anvil clouds from deep convective systems

Zhe Feng,¹ Xiquan Dong,¹ Baïke Xi,¹ Courtney Schumacher,² Patrick Minnis,³ and Mandana Khaiyer³

Received 22 June 2011; revised 28 September 2011; accepted 29 September 2011; published 6 December 2011.

[1] A new hybrid classification algorithm to objectively identify Deep Convective Systems (DCSs) in radar and satellite observations has been developed. This algorithm can classify the convective cores (CC), stratiform rain (SR) area and nonprecipitating anvil cloud (AC) from the identified DCSs through an integrative analysis of ground-based scanning radar and geostationary satellite data over the Southern Great Plains. In developing the algorithm, AC is delineated into transitional, thick, and thin components. While there are distinct physical/dynamical differences among these subcategories, their top-of-atmosphere (TOA) radiative fluxes are not significantly different. Therefore, these anvil subcategories are grouped as total anvil, and the radiative impact of each DCS component on the TOA radiation budget is quantitatively estimated. We found that more DCSs occurred during late afternoon, producing peak AC fraction right after sunset. AC covers 3 times the area of SR and almost an order of magnitude larger than CC. The average outgoing longwave (LW) irradiances are almost identical for CC and SR, while slightly higher for AC. Compared to the clear-sky average, the reflected shortwave (SW) fluxes for the three DCS components are greater by a factor of 2–3 and create a strong cooling effect at TOA. The calculated SW and LW cloud radiative forcing (CRF) of AC contribute up to 31% of total NET CRF, while CC and SR contribute only 4 and 11%, respectively. The hybrid classification further lays the groundwork for studying the life cycle of DCS and improvements in geostationary satellite IR-based precipitation retrievals.

Citation: Feng, Z., X. Dong, B. Xi, C. Schumacher, P. Minnis, and M. Khaiyer (2011), Top-of-atmosphere radiation budget of convective core/stratiform rain and anvil clouds from deep convective systems, *J. Geophys. Res.*, 116, D23202, doi:10.1029/2011JD016451.

1. Introduction

[2] Cirrus clouds are known for their frequent occurrence and globally large areal coverage, and have strong influence on climate changes through their effects on the surface and top-of-atmosphere (TOA) radiation budgets [Liou, 1986]. Generally located at high altitudes in the troposphere, these ice clouds reduce the amount of solar radiation reaching the earth's surface by reflection and modify outgoing longwave radiation (OLR) at TOA through absorption. Their net radiative effect varies with the surface and atmospheric conditions below, as well as the cirrus macrophysical and microphysical properties [Stephens, 2005]. Cirrus clouds, particularly those associated with deep convective systems (DCSs), are also found to have a dynamic connection with moisture fields in the upper troposphere [e.g., Soden, 2000; Soden et al., 2004; Dessler and Sherwood, 2000].

[3] DCSs have traditionally been divided into the deep convective precipitating portion and the nonprecipitating anvil canopy. The former is important to the atmospheric hydrologic cycle because of the heavy precipitation in the convective cores (CC) and widespread precipitation in the stratiform rain (SR) regions, and the latter is dominant in the atmospheric radiation budget due to their extensive spatial coverage. Satellite observations have been widely used to examine the radiative impact of DCSs [e.g., Machado and Rossow, 1993; Del Genio and Kovari, 2002]. Debates on whether tropical DCS have positive or negative radiative feedback further highlight their importance to the earth's climate system [Hartmann et al., 2001; Lindzen et al., 2001; Lin et al., 2002, 2004, 2006]. Many of the techniques used to separate the precipitating convective and nonprecipitating anvil regions of a DCS are based simply on infrared (IR) brightness temperature thresholds [e.g., Machado and Rossow, 1993; Lin et al., 2006]. While the IR-based satellite method can identify the general location of the precipitating portion of a DCS through its cold brightness temperature, the heaviest precipitation (i.e., CC) does not always correspond to instantaneous overlying cold cloud tops during the mature stage of the DCSs [Pandya and Durran, 1996; Yuter and Houze, 1998; Rickenbach, 1999]. The complex evolution of DCSs and their similar

¹Department of Atmospheric Sciences, University of North Dakota, Grand Forks, North Dakota, USA.

²Department of Atmospheric Sciences, Texas A&M University, College Station, Texas, USA.

³NASA Langley Research Center, Hampton, Virginia, USA.

cloud top properties observed from passive satellite optical sensors make it difficult to isolate cirrus anvil clouds (AC) from their CC and to study their spatial patterns and evolution, which leads to uncertainties in estimating the radiative impact of the associated AC.

[4] Radar observations have led to better characterization of the precipitation structure of DCS, particularly for meso-scale convective systems (MCS; see Houze [2004] for a review). These systems typically contain a large region of stratiform precipitation, accompanied with an extensive upper level cirrus cloud shield [Houze *et al.*, 1980, 1989; Houze, 1993, 1997]. While heavy rain and graupel developed in intense convective updrafts fall out directly downward and appear as reflectivity cores (or “convective cells”) on radar, more moderately sized ice particles remain in middle and upper troposphere and spread laterally, ultimately forming SR and AC [Houze, 2004]. Several recent satellite-based studies have focused on developing new techniques to better characterize the nonprecipitating tropical MCS AC. Li and Schumacher [2011] used 10 years of Tropical Rainfall Measurement (TRMM) Precipitation Radar (PR) data to investigate thick anvil and its relationship to convective strength. Due to the low sensitivity of the TRMM PR, they showed that their results underestimated anvil top height by an average of 5 km and underestimated anvil horizontal extent by a factor of 4. By manually tracking geostationary satellite images and TRMM PR observations to determine the existence of an MCS, Cetrone and Houze [2009] separated the anvil portions using collocated CloudSat Cloud Profiling Radar data and analyzed the anvil vertical structure. Yuan and Houze [2010] developed an objective technique to identify MCSs and separated their anvils by combining data from several A-train satellite instruments. They mapped MCSs over the entire tropics and further characterized the horizontal and vertical structures of their anvils.

[5] While MCSs account for a majority of tropical rainfall, smaller storms occur more often than MCSs and thus contribute significantly to the radiative budget [e.g., Machado and Rossow, 1993; Machado *et al.*, 1998; Del Genio and Kovari, 2002; Nesbitt *et al.*, 2006]. Zeng *et al.* [2009a, 2009b] used long-term cloud-resolving model simulations to investigate the effect of ice cloud microphysics on the TOA radiative flux between the midlatitudes and tropics. They found that the upper tropospheric cloud ice content and TOA radiative forcing are more sensitive to ice nuclei in the midlatitudes than in the tropics. This is because ice nuclei have a stronger impact on cloud ice crystals than on graupel. The former exist mainly in SR and AC while the latter dominates in CC. However, their model-simulated radiative fluxes were only compared with total observed fluxes, because up to now it has been difficult to separate SR from nonprecipitating AC using observations.

[6] Accurate separation of AC from the precipitating center of DCSs may also benefit spaceborne precipitation retrievals. Precipitation retrievals from satellite can be based on geostationary satellite IR observations [e.g., Kuligowski, 2002; Hong *et al.*, 2004], passive microwave measurements from polar-orbiting satellites [Kummerow *et al.*, 2001] and the TRMM PR [Kummerow *et al.*, 2000]. While microwave and radar-based methods provide more robust rainfall rates, they suffer from poor temporal resolution for any given location (~2 times per day per satellite). On the other hand,

geostationary IR-based techniques provide almost continuous precipitation retrievals for a specific region, but the weak relationship between cloud top IR temperature and the near-surface rainfall rate reduces their reliability. Vicente *et al.* [1998] suggested that effective screening of nonraining AC from rain cores is crucial to the accuracy of IR-based retrieved rainfall.

[7] In this study, we have developed a method to objectively identify DCSs and subsequently classify their CC, SR regions, and AC through an integrative analysis of collocated ground-based scanning radar and geostationary satellite data over the Southern Great Plains (SGP) region. Compared to polar orbiting satellites, ground-based radar and geostationary satellites can provide both spatial and temporal resolutions over the SGP region to resolve the diurnal cycle of DCSs. Detailed and accurate classification of the DCS components described in this paper can be used to better quantify their impact on TOA radiation, to improve the screening of DCS AC from precipitating cores for geostationary satellite precipitation retrieval, and to provide quantitative mapping of anvils for studying their morphology and life cycles. The present study focuses on quantifying the radiative fluxes at the TOA from these DCS components and estimating their cloud radiative forcing (CRF). This paper is organized as follows: Section 2 introduces various data sets; section 3 describes the hybrid classification algorithm to objectively identify DCSs and classify each component from the DCSs using the combined ground radar and geostationary satellite data sets; section 4 shows the statistical results of the three classified DCS components and their associated cloud radiative forcing over the SGP region during the period June–August 2009–2010; and section 5 summarizes our findings.

2. Data

[8] The two main data sets used in this study are from the Next-Generation Radar (NEXRAD) network and the 11th Geostationary Operational Environmental Satellite (GOES) located at 135°W. The study domain covers 8° latitude (32–40°N) by 14° longitude (91–105°W) over the SGP in the United States. We analyzed data for two summer seasons (June–August) in 2009 and 2010.

2.1. NEXRAD 3D Mosaic

[9] The ground-based scanning radar data were obtained from the National Severe Storms Laboratory National Mosaic and MultiSensor QPE (NMQ) project [Zhang *et al.*, 2011]. Raw radar reflectivity data in spherical coordinates from a single NEXRAD system were first quality controlled, and objectively projected onto a 3-D regular Cartesian space. Each single radar Cartesian grid centered at the radar site encompasses either 460 km radar umbrella (for coastal radars and radars located along the U.S.–Canada and U.S.–Mexico boundaries) or 300 km radar umbrella (for inland radars) [Zhang *et al.*, 2006]. The single radar grids are then merged using additional spatial and temporal weighting schemes to produce a unified 3-D grid covering the contiguous United States, from 20°N to 55°N latitudes between 130°W and 60°W longitudes, with a specific focus on minimal smoothing to the radar data [Zhang *et al.*, 2005; Langston *et al.*, 2007]. The NMQ 3D Mosaic reflectivity data set has fix 0.01° (~1 km) horizontal resolution, 0.5 km

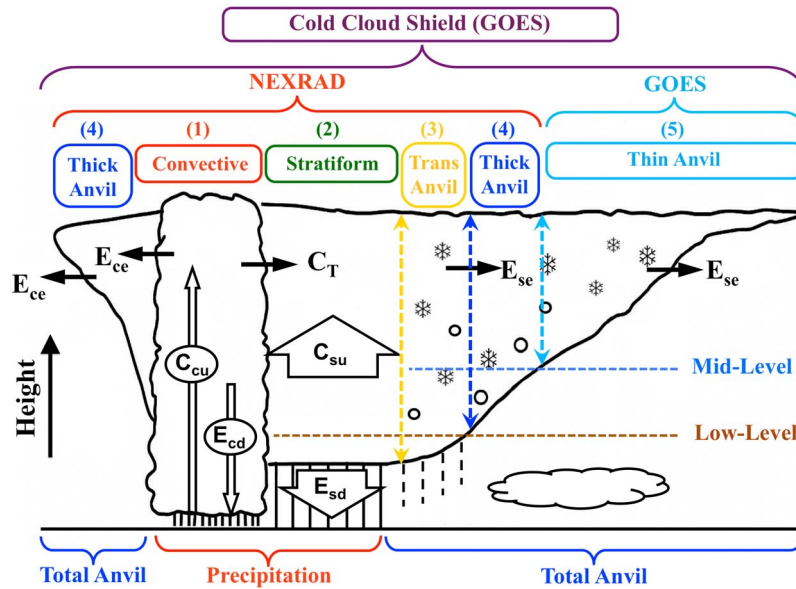


Figure 1. Schematic vertical cross section of a deep convective system with each of its components and observing platforms labeled. Four components, (1) convective core, (2) stratiform rain, (3) transitional anvil, and (4) thick anvil, are classified by NEXRAD radar, and the remaining (5) thin anvil is classified by GOES satellite. Low-level and midlevel heights are for demonstration purpose and not scaled to actual height. This schematic was adapted from *Frederick and Schumacher* [2008] and has been modified to include thin anvils from satellite observations.

vertical resolution everywhere up to 18 km above mean sea level (MSL), and 5 min temporal resolution.

2.2. GOES

[10] The GOES-retrieved cloud and radiation properties used in this study were obtained from the Atmospheric Radiation Measurement Program (ARM) [Ackerman and Stokes, 2003] data archive center. The GOES cloud products, summarized by *Ayers et al.* [2006], were retrieved using the algorithms developed for the NASA Clouds and the Earth's Radiant Energy System (CERES) project [Minnis et al., 2008, 2011]. Three specific products were used in this study: 10.8 μm channel brightness temperature (T_{IR}), retrieved cloud top (Z_{top}) and cloud base (Z_{base}) heights, and OLR and shortwave albedo. The retrieval methods are briefly described in the following paragraphs.

[11] The cloud properties, phase, effective temperature, optical depth, and particle effective size were retrieved half-hourly for 4 km pixels using the 0.65, 3.9, 10.8, and 11.9 μm channels in the Visible Infrared Shortwave-infrared Split-window Technique (VISST) for daytime, and the Shortwave-infrared Split-window Technique (SIST) for nighttime [Minnis et al., 2011]. Cloud effective temperature, which corresponds to the radiating center of the cloud, is used to define the cloud effective height. The cloud effective height is determined using the lowest altitude where the atmosphere-corrected T_{IR} matches a vertical temperature profile. The Rapid Update Cycle (RUC) analyses [Benjamin et al., 2004] were used to represent the vertical atmospheric temperature profile above 500 hPa, while a surface-temperature-anchored lapse rate defines the temperature profile at lower altitudes as described by Minnis et al. [2011]. For optically thick clouds (optical depth >6), cloud top height

is assumed to be close to the cloud effective height and is computed using a local temperature profile from RUC [Smith et al., 2008]. Cloud thickness was estimated using empirical fits with several parameters such as cloud optical depth, effective temperature, and particle effective diameter for different types of clouds [Minnis et al., 2011]. Cloud base height is the difference between cloud top altitude and cloud thickness.

[12] The GOES broadband (BB), shortwave (SW), and longwave (LW) fluxes were derived using empirical narrow-band (NB) to BB conversion functions. The CERES-measured BB fluxes were matched with and regressed against GOES NB fluxes to derive the conversion coefficients for each band as reported by *Khayer et al.* [2006, 2011] using updates of the methods described by Minnis et al. [1995]. Relative to the 2008–2009 CERES Terra Edition-2 Rev1 fluxes, the SW albedo and OLR from GOES-11 have RMS errors of 6.5 and 3.0%, respectively [Khayer et al., 2011].

3. Description of the Hybrid Classification Algorithm

3.1. Defining DCS Structure

[13] Figure 1 shows the schematic for an idealized DCS structure and the definition of each of its components, which are classified by combining two data sources. We use the collocated GOES-NEXRAD observations to objectively identify a DCS and further separate the precipitating and anvil cloud (AC) components as illustrated in Figure 1. The methodology for identifying the DCS components is discussed in detail in sections 3.2 to 3.4. For an identified DCS cloud patch, a total of five components are defined as follows by NEXRAD (components 1–4) and GOES (component 5):

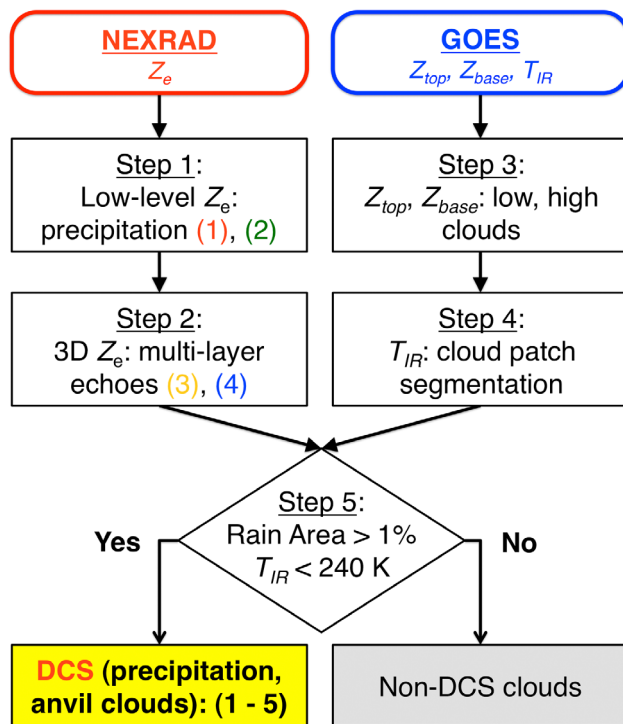


Figure 2. Flowchart of the hybrid classification algorithm used in this study.

(1) convective core (CC): strong, vertically oriented reflectivity maximum that produces intense precipitation, with contiguous echo top above 6 km; (2) stratiform rain (SR): widespread precipitation that has a weak horizontal reflectivity gradient and (at times) enhanced reflectivity near the 0°C level called the bright band; must also have contiguous echo top above 6 km; (3) transitional anvil: neither convective nor stratiform rain, but contiguous vertical reflectivity with an echo base below 3 km (low level) and an echo top above 6 km (midlevel), representing the transition region from precipitating cloud to nonprecipitating anvils (selection of low-level and midlevel heights is explained in section 3.2); (4) thick anvil: radar reflectivity that has an echo base above low level; and (5) thin anvil: cloud top heights above the midlevel observed by GOES, but not by NEXRAD.

[14] While the separation of CC and SR from radar has been well established [Churchill and Houze, 1984; Steiner *et al.*, 1995], the definition of the anvil region is unclear. Previous studies have used elevated upper-level echoes (i.e., echo base above a certain height) from cm wavelength radars to define anvils [e.g., Frederick and Schumacher, 2008; Li and Schumacher, 2011]. Elevated radar echoes from a DCS, particularly those attached to the CC (as illustrated adjacent to the CC in Figure 1), have been shown as a good proxy for estimating convective mass transport and detrainment [Mullendore *et al.*, 2009]. Examination of the vertical reflectivity profile composites in the Transitional Anvil region (not shown) reveals that reflectivities below the melting layer are substantially lower than that in the SR region. Oklahoma Mesonet surface rain gauge measurements indicate that the frequency of measurable precipitation (>0.1 mm in any 5 min interval) at the surface in the Transitional Anvil region is only 6%, compared

to 26% in the SR region. Our ongoing research also reveals that there are significant differences in the vertical velocity profiles between Transitional Anvil and Thick Anvil, suggesting that Transitional Anvils are possibly remnants (or precursors) of stratiform precipitation and may be dynamically different from both the SR region and elevated anvils. Due to these distinct physical/dynamical differences, Transitional Anvil and Thick Anvils are defined as two different categories in the radar classification output for future DCS anvil studies.

[15] The operational NEXRAD radar product is mainly designed for monitoring weather events and providing quantitative precipitation estimates. The capability of detecting clouds using the operational NEXRAD product is limited by many factors such as scanning strategy, and vertical resolution and range from radars [Miller *et al.*, 1998; Feng *et al.*, 2009; Melnikov *et al.*, 2011]. It is expected that a significant portion of cirrus anvils, which mainly consist of smaller ice crystals, cannot be detected by NEXRAD due to its operational configuration and low sensitivity to nonprecipitating particles. Therefore, the remaining cirrus anvils are classified by analyzing the GOES data.

[16] Figure 2 shows the flowchart of the hybrid classification algorithm and data sets used for each step. The left-hand side of Figure 2 shows Steps 1 and 2 of the hybrid classification algorithm using NEXRAD observations, which determine the candidates for components 1–4 of the DCSs. The right-hand side of Figure 2 shows Steps 3 and 4 using GOES satellite observations to classify nonprecipitating clouds and to perform cloud patch segmentation. The final step jointly analyzes the output from both NEXRAD and GOES to identify DCSs and obtain the final hybrid classification output for components 1–5 of DCSs.

3.2. NEXRAD Radar Classification

[17] The first step of the radar classification starts with the convective/stratiform separation technique described by Steiner *et al.* [1995], which is a background exceeding technique using a low-level 2-D horizontal reflectivity field. Reflectivity at each radar grid is compared to its background intensity, computed using the linearly averaged reflectivity with a 6 km radius centered on the grid. If the reflectivity exceeds its background intensity threshold value, then it is assigned as convective. The threshold is a function of the background reflectivity value. Once the convective center is assigned, its surrounding grid points within an intensity-dependent convective radius around the center are also assigned as convective. The rest of the echoes that exceed 10 dBZ, but are not identified as CC, are designated as SR. The working level is chosen to be at 2.5 km above MSL, sufficiently below the 0°C level during summer to minimize bright band contamination. The absolute reflectivity threshold that a radar grid must exceed to be convective is set to 43 dBZ. The rain rate estimated from this reflectivity using the National Weather Service Z-R relationship ($Z = 300R^{1.4}$) for summer deep convection is approximately 20 mm h⁻¹. The classification output from step one is passed to the next step as precipitation flags.

[18] The second step of the radar classification utilizes the entire 3-D reflectivity structure to define multilayer echoes and classify Transitional Anvil and Thick Anvil areas. Low and middle layer heights are defined at 3 and 6 km above MSL, respectively, similar to those used by Dong *et al.*

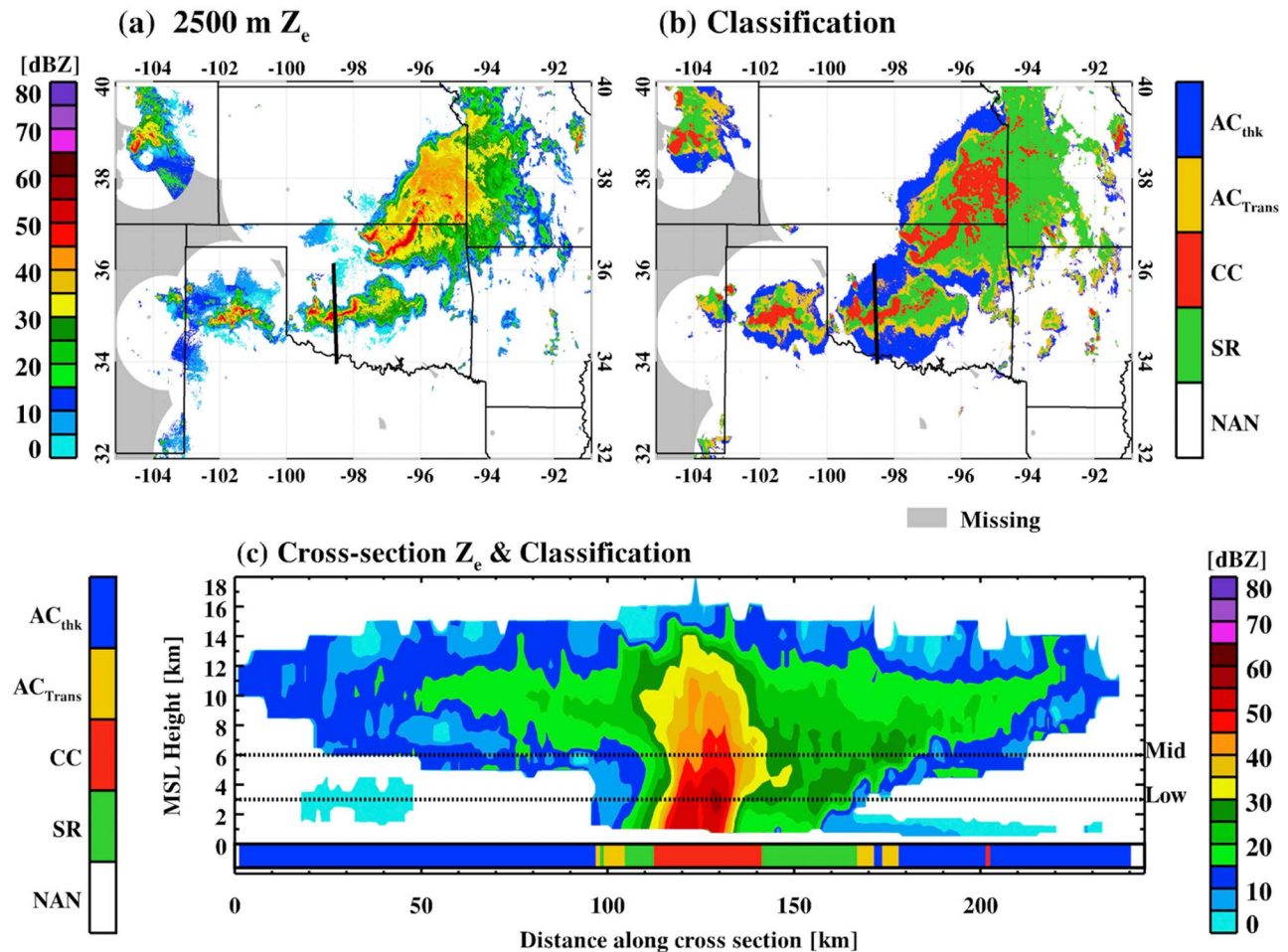


Figure 3. An example of the 3D radar classification over the study region (32–40°N, 91–105°W). (a) NEXRAD horizontal reflectivity at 2500 m MSL, the gray shaded areas near the western boundary represent no radar data at this height due to elevated terrain, (b) classified DCS components based on radar observations from surface to top, and (c) vertical cross section radar reflectivity, with the classification color-coded underneath. The cross section is taken along the black solid line in Figures 3a and 3b, and the two dashed lines in Figure 3c show the low-level and midlevel heights.

[2006]. These heights have been used previously to define low-level stratus clouds (below 3 km) and cirrus clouds (above 6 km). For each radar vertical column, a maximum of five echo layers are defined based on their echo base and top heights. An echo layer is defined as having contiguous reflectivity value above -10 dBZ with no more than one gap (0.5 km vertically). A radar grid is labeled as Transitional Anvil if a single layer echo base is below low-level height and echo top is above midlevel height. This definition is similar to that used by *Xi et al.* [2010]. If a single layer echo base is above low level and echo top is above midlevel, that radar grid is labeled as Thick Anvil. Finally, CC and SR from step one must have contiguous echo top above 6 km to maintain their precipitation flags. The multilayer echo identification does not require the low level to be echo free to identify anvil echoes, which is an improvement to handle ground clutter compared to the *Frederick and Schumacher* [2008] method.

[19] Figure 3 shows an example of the horizontal radar reflectivity and the radar classification results. As illustrated in Figure 3b, the precipitation area (red for CC and green for

SR) is mostly surrounded by Transitional Anvil (yellow) and Thick Anvil (dark blue). The cross section taken perpendicular to the DCS in central Oklahoma (Figure 3c) shows the vertical structure of the DCS with the classified components. Reflectivities below 3 km in the Transition Anvil region are significantly lower than SR region, suggesting possible virga. Note that between 20 and 50 km and 170–220 km along the cross section, the low level echoes do not affect the algorithm to correctly label the Thick Anvil category. The labeled components from the radar classification (i.e., Figure 3b) are used as candidates for the hybrid classification in step 5. However, the radar classification can be used in a stand-alone fashion for further investigations of Transitional Anvil and Thick Anvil associated with DCSs.

3.3. GOES Data Analysis

[20] The third step of the hybrid classification algorithm is to analyze GOES-retrieved cloud height data and label cloud clouds for each pixel by the three layers defined in section 3.2. A pixel is labeled as high cloud if its Z_{top} is above the midlevel and its Z_{base} is above low level. Similarly, if a

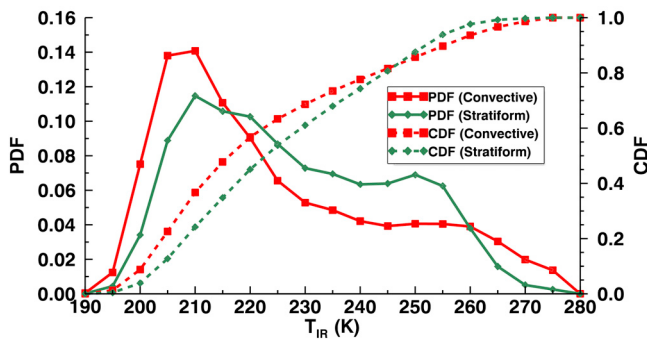


Figure 4. The probability distribution functions (PDF) and cumulative distribution functions (CDF) of the classified convective and stratiform regions from radar with the matched GOES IR temperatures over the study region during the summers (JJA) of 2009 and 2010.

pixel has Z_{top} below the low level, then it is labeled as low cloud. The GOES T_{IR} data are used to identify cold cloud shields (CCs), which are defined as cloud patches with T_{IR} colder than a threshold of 270 K. A warm temperature threshold has been used in previous studies to include a majority of the AC surrounding the colder precipitating cloud top interior of a DCS [e.g., Lin et al., 2006; Yuan and Houze, 2010]. The GOES cloud layer labeling ensures that no low-level clouds are misidentified as anvils. Sensitivity analyses show that using a colder cutoff temperature (e.g., 260 K used by Yuan and Houze [2010]) would not significantly affect the results in this study.

[21] After filtering out the clouds with T_{IR} warmer than 270 K, step 4 performs cloud patch segmentation on the remaining clouds with $T_{\text{IR}} < 270$ K. The procedure of this step is similar to that described by Hong et al. [2004]. The GOES T_{IR} field is first smoothed to prevent oversegmentation, then is segmented into individual cloud patches starting from the coldest cloud top center and moving outward to AC with warmer temperatures. All pixels within each segmented cloud patch are given a unique index for identification.

3.4. Determine DCS Using Both NEXRAD and GOES Outputs

[22] To spatially match the NEXRAD radar classification with GOES satellite data, a hybrid grid for these two data sets is produced. The hybrid grid domain is the overlapped area between the NEXRAD radar domain and the ARM SGP GOES domain, covering 32–40°N, 91–105°W, with a $0.04^\circ \times 0.04^\circ$ horizontal resolution. The original GOES 4 km pixel data are mapped onto the hybrid grid using the nearest neighbor method. This remapping does not introduce any significant shift of the original GOES data because of the similar resolution. The radar classification output from step 2 ($0.01^\circ \times 0.01^\circ$) is also aggregated onto the quarter-resolution hybrid grid. To represent the type for that hybrid grid, the most frequent type of 16 finer NEXRAD grids within a hybrid grid is used. Since the NMQ data product has a 5 min temporal resolution, the nearest 5 min radar output is used to match with the GOES data. The final NEXRAD and GOES hybrid data set is produced hourly.

[23] To determine whether a CCS is a DCS in the final step 5, the precipitation features from the radar classification

output in step 2 are combined with the GOES cloud patch segmentation in step 4 for analysis. Previous DCS life cycle studies used a threshold of ~ 240 K to track individual DCS and to indicate whether convective elements exist in high clouds [e.g., Maddox, 1980; Machado et al., 1998; Lin et al., 2006]. As demonstrated in those studies, using a cold T_{IR} center within a high cloud shield alone to identify DCS may overestimate the amount of precipitating clouds. On the other hand, using the radar classified near-surface precipitation alone may include shallow convection. Therefore, a joint analysis of radar and GOES output from steps 2 and 4 can better characterize a DCS. Figure 4 shows the probability distribution functions (PDFs) and cumulative distribution functions (CDFs) of the radar-classified convective and stratiform regions from step 2 with the matched GOES IR temperatures over the study area during the summers (JJA) of 2009 and 2010. To avoid partial bin filling issue, only hybrid grids that are completely filled with convective or stratiform type from radar are used in the calculation. This subset of data accounts for about 50% of all convective/stratiform samples. The number of observations from CC and SR are 1.04×10^6 and 3.08×10^6 , respectively. As demonstrated in Figure 4, 75% of all the CC and SR pixels are colder than 240 K, the remaining 25% are possibly related to the earliest stage of convective development or the late dissipating stage, or they are simply shallow convection. IR temperature PDFs from Transitional Anvil and Thick Anvil (not shown) are very similar to that from CC and SR, which is consistent to the results of Yuter and Houze [1998] in that cold cloud top IR temperatures do not always correspond to precipitation near the surface.

[24] To quantify the radiative impact from all sizes of DCSs that are observed by GOES satellite, and to include as many of the developing and dissipating DCS stages as possible, 240 K was chosen as the cold center temperature threshold to indicate convective elements within a CCS. This IR temperature threshold approximately corresponds to the 10 km cloud top height from the GOES retrieval. Conducting a sensitivity test using different temperature thresholds from 235 K to 245 K changed the estimated radiative fluxes by only a few percent, suggesting that the exact value of the temperature threshold is not important within this range.

[25] A CCS is hereby defined to be a DCS by this standard: within a CCS patch, if the precipitating area (CC and/or SR) overlaps with the cold cloud top center ($T_{\text{IR}} < 240$ K) for more than 1% of the CCS patch area, that CCS is considered a DCS patch. We chose a low area percentage because we want to ensure the statistical results include not only mature DCSs, whose large precipitating area overlaps with cold cloud top temperatures, but also developing and dissipating DCSs. If a higher area percentage is used, the dissipating stage of DCSs is often missed because most of the remaining upper level clouds at this stage are not precipitating.

[26] Figure 5 shows an example of the DCS identification and classification steps along with the final output. After the cloud patch segmentation process is performed on a GOES T_{IR} field (Figure 5a), precipitation features (Figure 5b) are analyzed in conjunction with T_{IR} for each cloud patch, and the patches that satisfying the DCS definition described above are then labeled (color patches in Figure 5c). The final step of the analysis is performing the hybrid classification on

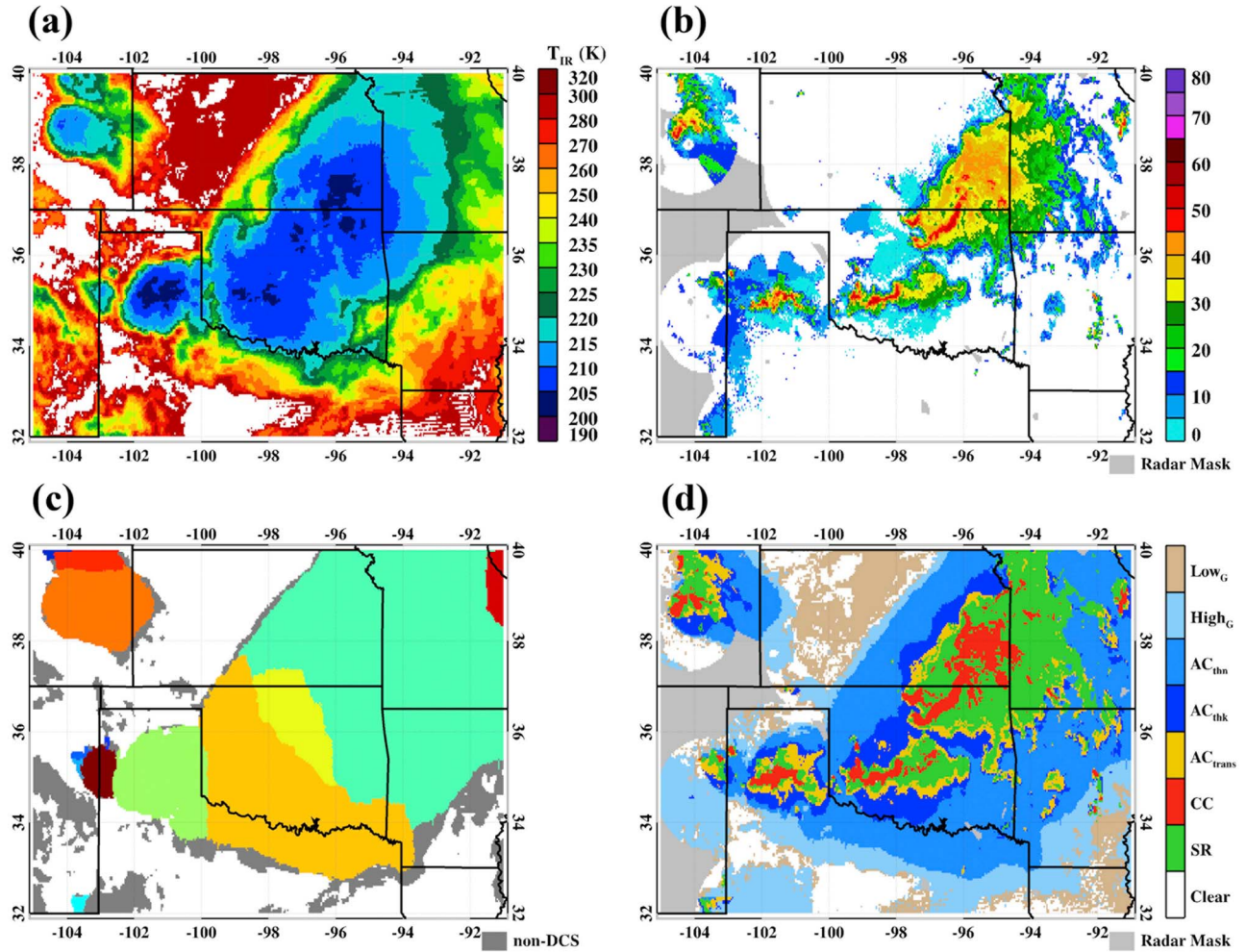


Figure 5. An example of the hybrid classification process. (a) GOES IR temperature, (b) NEXRAD radar reflectivity aggregated onto the hybrid grid, and (c) cloud patch segmentation; the color patches are identified as deep convective systems (DCSs) and the gray patches are other high clouds; both GOES IR temperature and NEXRAD indicated precipitation features are used to identify DCSs. (d) The final hybrid classification output.

the identified DCS patches. For a DCS patch, all four categories from the radar classification candidates maintain their class type, and additional GOES identified high cloud pixels ($Z_{\text{top}} > 6$ km) within the DCS patch are labeled as Thin Anvil (Figure 5d). Other cloud patches (gray color in Figure 5c) and other type of clouds (e.g., non-DCS associated High and Low Clouds in Figure 5d) that do not meet the DCS requirements are not included in the follow sections.

4. Application of the Hybrid Classification Algorithm

[27] The hybrid classification algorithm described in the previous section was applied to NEXRAD and GOES data for six summer months (June–August, 2009 and 2010). The statistics were calculated within the hybrid grid domain (32–40°N, 91–105°W). We note that the differences in the physical (e.g., optical depth, particle size) and dynamical (e.g., vertical velocity) characteristics between Transitional Anvil, Thick Anvil and Thin Anvil are important to other

applications, such as improving the screening of non-precipitating anvil cloud (AC) from geostationary satellite data and DCS anvil life cycle studies. However, for the purpose of estimating TOA radiative fluxes in this study, these three components classified by the algorithm were grouped as Total Anvil, and compared with those from Convective Core (CC) and Stratiform Rain (SR).

[28] Figure 6 shows the diurnal cycle of the three main components from DCSs in the data set. The frequency of occurrence (FREQ, Figure 6a) is the ratio of the number of times each of three DCS components was identified by the hybrid classification algorithm, to the total number of available observations over the study domain during that hour. Small DCSs consisting only of a few pixels are meaningless for calculating the TOA radiation budget over the study domain. To avoid them, a threshold of 0.01% of the domain area ($\sim 111 \text{ km}^2$) covered by each of the three DCS components is required for a DCS to be included in the Frequency counting. As illustrated in Figure 6a, FREQs of the three DCS components decrease monotonically from

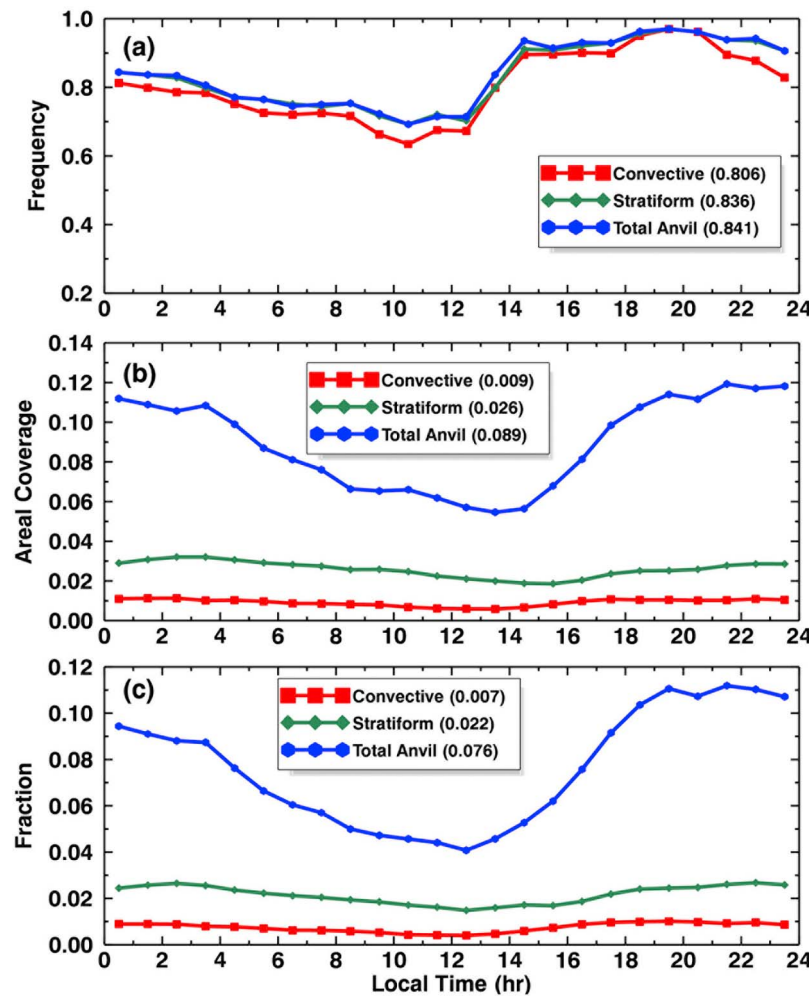


Figure 6. Hourly mean diurnal cycles of DCS convective core, stratiform rain and total anvil (transitional anvil + thick anvil + thin anvil in Figure 1) over the study domain during the period June–August, 2009–2010. (a) Frequency of occurrence, (b) areal coverage, and (c) fraction (frequency \times coverage). Values in the parentheses are average values over the study domain.

midnight to local noon, and then increase and reach maxima around late afternoon (~ 1900 LT). This diurnal cycle suggests that most of the DCSs over the SGP region are triggered between early and late afternoon as a result of increased solar heating at the surface and mixing at the boundary layer [Carbone *et al.*, 2002].

[29] The areal coverage (Figure 6b) is simply the ratio of the number of pixels classified as one of the three DCS components to the total number of pixels within the study domain during that hour. Compared to AC, the areal coverage of both CC and SR are much smaller, and their diurnal cycles are much weaker. Examination of averaged DCS sizes (not shown) suggests that high DCS frequency hours (afternoon) are commonly associated with small convective cells. SR area increases when individual convective systems organized into MCSs from late afternoon to midnight that favors the growth of stratiform precipitation. The largest areal coverage of SR appears between 0200 to 0400 LT, and gradually decreases to a minimum by early afternoon. The areal coverage of AC shows a minimum at 1400 LT, and then increases at a rate of about $1\% \text{ h}^{-1}$ reaching a maximum value of 12% (approximately $1.37 \times 10^5 \text{ km}^2$) at about 2100

LT. The largest areal coverage of AC is most likely produced by nocturnal MCSs that are associated with large rain rates [Zhang and Klein, 2010]. Evaluation of GOES-retrieved cloud amount against ARM ground-based radar and lidar observations over the SGP region shows that GOES-derived cloud amount has excellent agreement with surface observations for both day and night [Dong *et al.*, 2006; Xi *et al.*, 2010; Kennedy *et al.*, 2010]. Thus, it is unlikely that the cloud detection differences between day and night introduce any significant diurnally dependent artifacts in this analysis.

[30] Domain fraction (Figure 6c) is the product of FREQ and areal coverage (i.e., fraction = FREQ \times areal coverage). Because the areal coverage of both CC and SR remains nearly constant throughout the entire day, the diurnal cycles of their domain fractions basically follow their FREQs but with much smaller magnitudes. SR fraction peaks at about 2200 LT, about 3 h behind CC. This delay is most likely associated with individual convective cells organized into larger convective complexes (i.e., MCSs) from late afternoon to early evening, producing peak SR and AC during late evening. The diurnal variation of AC fraction is similar to that of SR and peaks between 1900 and 2100 LT. These

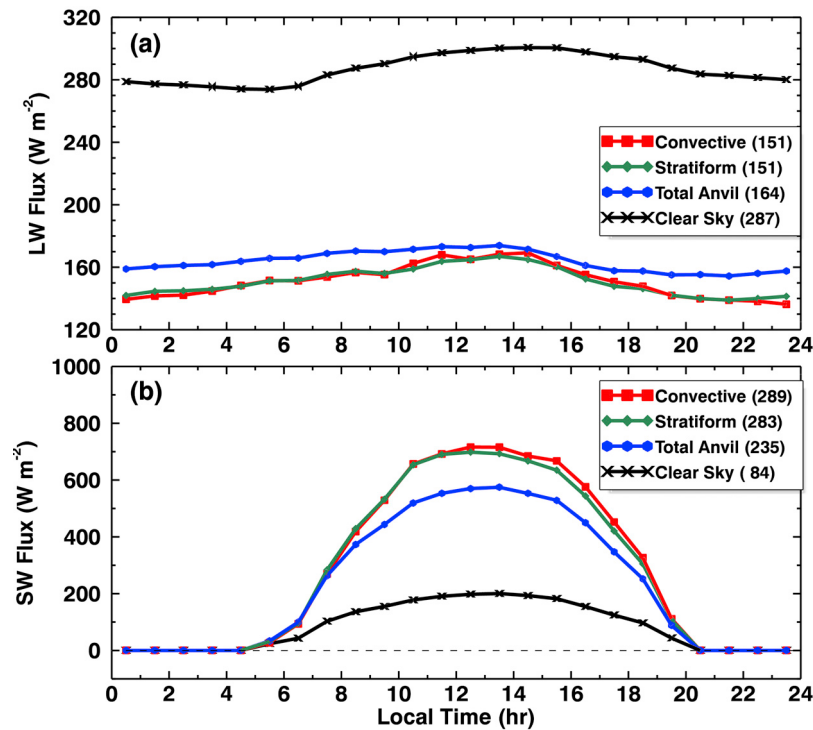


Figure 7. Same as Figure 6 except for TOA (a) Outgoing longwave radiation and (b) reflected shortwave (SW) flux for the classified three DCS components and clear-sky condition.

results are consistent with a recent study of transition mechanism from shallow to deep convection at the SGP, where locally triggered convection peaked in late afternoon and nocturnal MCSs peaked at and after midnight [Zhang and Klein, 2010]. To investigate the impact of DCSs and their three components on the TOA radiation budget, we also calculated the total cloud fraction over the study domain during the summers of 2009–2010. The average total cloud fraction is 0.45, consistent with previous studies [Dong *et al.*, 2006; Xi *et al.*, 2010; and Kennedy *et al.*, 2010]. We note that satellite retrieved ice cloud optical and microphysical properties are also important in assessment of DCS cloud radiative forcing due to their significant impact on radiative transfer model calculations [e.g., Yang *et al.*, 2007]. However, evaluating satellite derived microphysical properties in DCS clouds is beyond the scope of this study.

[31] Figure 7 shows the hourly mean TOA OLR and reflected SW fluxes for the three DCS components and for clear-sky conditions. The hourly mean clear-sky fluxes, averaged from all clear-sky pixels identified by the GOES cloud mask during that hour, represent the mean surface and atmospheric condition over the study domain during the summers of 2009–2010. The clear-sky OLR slightly decreases from midnight to early morning (0600–0700 LT), then starts to increase monotonically until early afternoon (1400 LT), and finally decreases to midnight. The clear-sky OLR pattern is mainly attributed to the skin temperature, which is highly dependent on total insolation at surface. This diurnal pattern is very similar to that of clear-sky downwelling LW flux at the SGP site [Dong *et al.*, 2006, Figure 4].

[32] The average OLR for CC, SR, and AC is 151, 151, and 164 W m^{-2} , respectively. The OLR uncertainties of the three DCS components have a range of 1–3% with a 95%

confidence interval. Differences in the average DCS OLR arise because CC and SR represent the coldest center of DCSs, while AC is slightly warmer but still represent cold cloud tops. As illustrated in Figure 7a, all three DCS components have a relatively small OLR diurnal variation. OLR increases slowly from midnight, reaches its maximum at around 1400 LT, and then gradually decreases to a minimum around midnight. This decrease in OLR from afternoon to midnight is consistent with growing convection during that time period. Comparing Figure 7 with Figure 6, we find that the diurnal variations of OLR for all three components almost mirror their variations in FREQ and fraction.

[33] The hourly mean reflected SW fluxes of clear sky and three DCS components during the summers of 2009–2010 are illustrated in Figure 7b. Compared to the clear-sky average of 84 W m^{-2} , the reflected SW fluxes for CC, SR, and AC are 289, 283, and 235 W m^{-2} , respectively, with an uncertainty of 2–3% for a 95% confidence interval. The DCS values are about a factor of 2–3 more than the clear-sky SW flux and create strong cooling at TOA. The strong cooling effect from CC and SR is expected because these clouds are optically thick. Reflected SW fluxes from CC and SR show a slight separation at midday but are almost identical in the early morning and early evening hours, suggesting that they both are highly reflective to solar radiation due to their higher optical depth. Furthermore, the reflected SW fluxes from DCS clouds are higher during afternoon than morning, resulting in asymmetric diurnal variations. These results suggest that newly formed DCS clouds during late afternoon are optically thicker and more reflective than those from dissipating DCSs in the morning.

[34] The TOA LW and SW CRFs of the three DCS components, weighted by their cloud fractions, are the differences

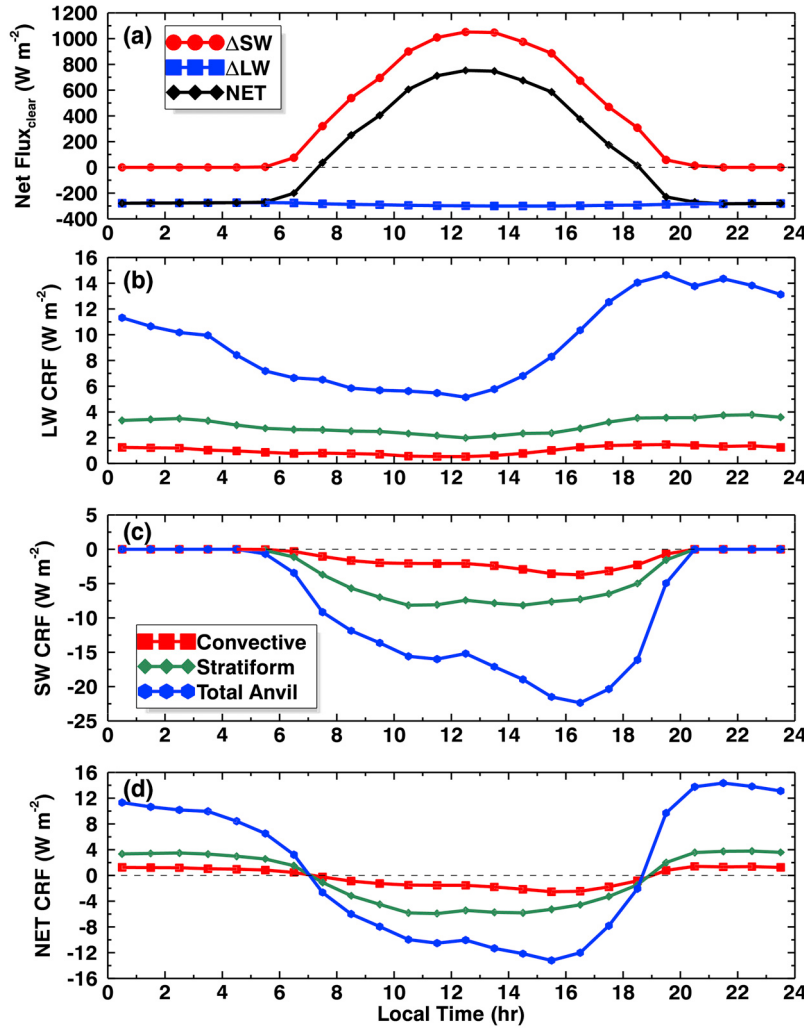


Figure 8. The hourly mean values of (a) clear-sky fluxes, (b) LW, (c) SW, and (d) NET cloud radiative forcings (CRFs) at TOA over the study domain. The LW, SW, and NET CRFs for three DCS components are weighted by their corresponding cloud fractions as shown in Figure 6.

between the net TOA fluxes (down-up) from cloudy sky (Q_{cloud} and F_{cloud}) and clear sky (Q_{clr} and F_{clr}) and are defined as

$$CRF_{SW} = \sum_i f_i (Q_{cloud}^i - Q_{clear})$$

and

$$CRF_{LW} = \sum_i f_i (F_{cloud}^i - F_{clear})$$

respectively, where f_i is the domain cloud fraction of each DCS component [Ramanathan, 1987; Ramanathan et al., 1989]. The NET CRF is the sum of CRF_{SW} and CRF_{LW} for each DCS component. Positive values of CRF indicate warming and negative values denote cooling of the entire earth-atmospheric column. Although the average fluxes from three DCS components differ significantly from clear-sky fluxes (Figure 7), their fractions, especially for CC, are relatively small compared to other nonconvective clouds (e.g., low-level stratus and synoptic cirrus clouds). Therefore the

calculated CRFs, weighted by their fractions, are much less than their fluxes.

[35] Figure 8 shows the hourly mean clear-sky OLR, absorbed SW, and NET fluxes and the calculated CRFs for the three DCS components. The CRFs are the products of the domain cloud fractions in Figure 6c and the flux differences between clear sky and each DCS component in Figure 7. Clear-sky OLR (Figure 8a) varies by only 29 W m^{-2} throughout the entire day with a minimum (-301 W m^{-2}) at 1400 LT and a maximum around midnight. Clear-sky absorbed SW flux basically follows the solar zenith angle. The average NET flux (SW + LW) for clear-sky condition during the two summer seasons is 89 W m^{-2} (downward).

[36] Clouds associated with deep convection significantly alter the radiative flux into and out of the earth system. Although the flux differences between clear sky and CC/SR are significantly larger than those between clear sky and AC, the AC fraction is 3 times that of SR and almost an order of magnitude greater than CC. As a result, both the LW and SW CRFs of AC are much larger than those of CC and SR, as shown in Figure 8. Because of small variations in OLR from

Table 1. Averages of Cloud Fractions and Their Weighted TOA CRFs Over the Study Domain During the Period June–August, 2009–2010^a

	Fraction (Domain)	LW CRF (Wm ⁻²) (%)	SW CRF (Wm ⁻²) (%)	NET CRF (Wm ⁻²) (%)
Total Cloud	0.447	25.2	-32.9	-7.7
Convective Core	0.007	1.0 (4.1)	-1.2 (3.8)	-0.2 (3.9)
Stratiform Rain	0.022	2.9 (11.6)	-3.6 (10.8)	-0.6 (11.2)
Total Anvil	0.076	9.4 (37.3)	-8.6 (26.2)	0.8 (31.0)
Entire DCS	0.105	13.4 (52.9)	-13.4 (40.6)	0.0 (46.0)

^aNumbers in parentheses are the percentages of DCS and its three components' contribution to total cloud CRFs. Percentages are calculated using absolute flux values.

DCS clouds, the LW CRFs (Figure 8b) mimic the diurnal cycle of their fractions (Figure 6c). That is, the maximum warming from AC occurs right after sunset, when AC fraction peaks before gradually decreasing from early evening to local noon, when convection dissipates. Both CC and SR show a similar pattern but with much smaller magnitudes.

[37] SW CRFs (Figure 8c) show asymmetric patterns between morning and afternoon hours due to the onset timing of DCSs. Cooling from AC peak at around 1600 LT when convection is intense and solar radiation drops off sharply. The CC SW CRF has a similar pattern to that of AC, but is almost an order of magnitude lower. SR, on the other hand, shows stronger cooling in the morning than in the afternoon, consistent with reduced SR fractions during convective development in the early afternoon. The NET CRFs (Figure 8d) for DCS clouds mainly follow their SW CRFs during daytime, and are determined by their LW CRFs during the night. The strong cooling during daytime and warming during nighttime from AC almost cancel each other out, resulting in a slight warming of 0.8 W m^{-2} (Table 1). While the net radiative effects from AC are relatively small at TOA, the SW cooling impacts the surface due to small absorption of SW radiation in the atmosphere. This SW cooling may act to stabilize the surface and suppress convection development near the anvil region. On the other hand, radiative transfer model calculations suggested that local warming at the lower part of anvil due to absorption of upcoming LW radiation, and cooling at the top tend to destabilize the thermal structure of the middle atmosphere, which may reinforce mesoscale circulations and partially maintain the cloud deck via lifting [Webster and Stephens, 1980; Machado and Rossow, 1993]. This LW warming would reduce the cooling effect discussed above and the net radiative impact of DCS on dynamics.

[38] Table 1 shows the average domain cloud fraction and LW, SW, and NET CRFs from the three DCS components along with the percentage contribution to the total CRF. Absolute flux values were used to calculate the percentage contributions to total CRF. The NET CRFs of SR and AC contribute up to 11 and 31% of total NET CRF, while CC only contributes 4%. The remaining CRFs are associated with non-DCS clouds. When all clouds associated with DCSs are considered, their SW and LW CRFs contribute 53 and 41% of total SW and LW CRFs, respectively. The net TOA radiative effect from the sum of CC, SR, and AC is zero. Previous studies over the deep tropics reported small net cooling effect from DCS cluster ensembles, suggesting a feedback mechanism driving the net radiation in convective

region toward adjacent nonconvective areas [Hartmann *et al.*, 2001]. The zero net radiation in our result suggests a neutral influence on the feedback for midlatitude DCSs. Therefore, radiative feedbacks from summertime midlatitude clouds could instead be decided by non-DCS clouds. To examine the surface and atmospheric radiative budgets for DCS and non-DCS clouds, it is necessary to collocate the surface and satellite observations [Dong *et al.*, 2006, 2008].

5. Summary and Conclusions

[39] A new hybrid classification algorithm to objectively identify DCSs has been developed. This algorithm can separate the convective core (CC), stratiform rain (SR), and anvil cloud (AC) regions from the identified DCSs through an integrative analysis of collocated ground-based scanning precipitation radar and geostationary satellite data over the SGP region. In developing the algorithm, AC clouds are further delineated into transitional, thick and thin anvils due to their physical/dynamical differences and the limitations from radar and satellite sensors. While the TOA radiation budget of these regions is not significantly different, the algorithm can be used in future DCS anvil studies. For the purpose of this study, these three anvil subcategories are grouped as total anvil (i.e., AC). To that end, the radiative fluxes at TOA are then separated into CC, SR, and AC and the cloud radiative forcings are calculated, resulting in the first quantitative estimates of the radiative impact of each DCS component on the TOA radiation budget. Applying the hybrid classification algorithm to the NEXRAD and GOES data over the study region (32–40°N, 91–105°W) during the period June–August, 2009–2010, we have the following statistical results.

[40] 1. The frequencies of occurrence for the classified CC, SR, and AC decrease monotonically from midnight to local noon, and then increase and reach maxima around late afternoon. This diurnal cycle suggests that most of the DCSs over the SGP region are triggered between early and late afternoon as a result of increase solar heating at the surface and mixing at the boundary layer. The areal coverage of both CC and SR are much smaller and their diurnal cycles are much weaker than those of AC. The diurnal cycles of their domain fractions basically follow their frequency of occurrence but with much smaller magnitudes.

[41] 2. The clear-sky OLR slightly decreases from midnight to early morning, then starts to increase monotonically until early afternoon, and finally decreases to midnight. The average OLR for CC, SR, and AC is 151, 151, and 164 W m^{-2} , respectively. The CC and SR represent the coldest center of DCS, while AC is slightly warmer. All three DCS components have relatively small OLR diurnal variations, and their patterns almost mirror the variations of their FREQs and fractions. Compared to the clear-sky average of 84 W m^{-2} , the reflected SW fluxes for CC, SR, and AC are 289, 283, and 235 W m^{-2} , respectively. The DCS values are greater by a factor of 2–3 than the clear-sky conditions and create strong cooling at TOA.

[42] 3. Although the flux differences between clear sky and CC/SR are significantly larger than those between clear sky and AC, the AC fraction is 3 times that of SR and an order of magnitude greater than CC. As a result, both LW and SW CRFs of AC are much larger than those of the CC

and SR. The average LW, SW, and NET CRFs from the three DCS components along with their percentage contribution to the total CRF are summarized in Table 1. The NET CRF of SR and AC contribute up to 11 and 31% of total NET CRF, respectively, while CC only contributes 4%. When all clouds associated with DCS are considered, their SW CRF and LW CRF contribute 53 and 41% of total SW and LW CRFs, respectively. A net zero CRF for all DCS associated clouds suggest a neutral influence on DCS radiative feedback in the midlatitude summer.

[43] The hybrid classification has been used to quantify the impact on TOA radiation budget from each of the DCS components in this study. Although the algorithm is developed for ground-based NEXRAD radar systems and GOES satellite during summer time period over midlatitudes, the method can be used in other locations such as the tropics with minor modification of certain thresholds. For example, the radar classification algorithm can be applied on other scanning precipitation radars (S- or C-band), because the original Steiner *et al.* [1995] convective/stratiform partitioning was developed for data set from tropical radars. IR brightness temperature measurements are also available from many optical satellite sensors. The algorithm can be relaxed without the dependence on cloud height retrievals, similar to that described by Yuan and Houze [2010], and hence be applied to any satellite sensors with an IR channel. A feasible and important application would be on the TRMM satellite data set. Because convective/stratiform partitioning and 3-D reflectivity field are standard operational products from TRMM PR, and T_{IR} data are available from the TRMM Visible Infrared Scanner, this algorithm can potentially be used for global climate data synthesis.

[44] Detailed separation between various AC types and the precipitating center of DCSs has other important applications, such as evaluating and improving geostationary satellite IR-based precipitation retrievals and DCS lifecycle studies. Differences in satellite retrieved cloud properties (e.g., optical depth, particle size) between precipitating cores and AC identified by this method can be used to better screen out nonraining clouds, which has been a major difficulty in IR-based retrievals [Vicente *et al.*, 1998; Kuligowski, 2002]. By incorporating 3-D reflectivity and precipitation provided by the NMQ NEXRAD product with an objective satellite tracking method [e.g., Futyant and Del Genio, 2007], the relationship between parent convective strength and AC structures can be obtained throughout the DCS lifecycles to improve our understanding of the morphology of convective AC. A follow-up paper addressing these topics is underway.

[45] **Acknowledgments.** We would like to thank Ed Zipser, Bing Lin, and an anonymous reviewer for their constructive comments and suggestions in improving the manuscript. Carrie Langston at the National Severe Storm Laboratory provided invaluable help in the NEXRAD NMQ data product. This research was primarily supported by NASA Energy and Water Cycle Study (NEWS) project managed by Jared Entin. The University of North Dakota authors were supported by NEWS project under Grant NNX07AW05G, and supported by NASA CERES project under grant NNX10AI05G. The satellite analyses were also supported by DOE Office of Science, Office of Biological and Environmental Research, through contract DE-AI02-07ER64546.

References

- Ackerman, T. P., and G. M. Stokes (2003), The Atmospheric Radiation Measurement Program, *Phys. Today*, 56(1), 38, doi:10.1063/1.1554135.
- Ayers, J. K., et al. (2006), Overview of NASA Langley ARM cloud products and validation, paper presented at 16th ARM Science Team Meeting, U.S. Dep. of Energy, Albuquerque, N. M., March 27–31. [Available at http://www.arm.gov/publications/proceedings/conf16/extended_abs/ayers_jk.pdf.]
- Benjamin, S. G., et al. (2004), An hourly assimilation–forecast cycle: The RUC, *Mon. Weather Rev.*, 132(2), 495–518, doi:10.1175/1520-0493(2004)132<0495:AHACTR>2.0.CO;2.
- Carbone, R. E., J. D. Tuttle, D. A. Ahijevych, and S. B. Trier (2002), Inferences of predictability associated with warm season precipitation episodes, *J. Atmos. Sci.*, 59(13), 2033–2056, doi:10.1175/1520-0469(2002)059<2033:IOPAWW>2.0.CO;2.
- Cetrone, J., and R. A. Houze (2009), Anvil clouds of tropical mesoscale convective systems in monsoon regions, *Q. J. R. Meteorol. Soc.*, 135(639), 305–317, doi:10.1002/qj.389.
- Churchill, D. D., and R. A. Houze (1984), Development and structure of winter monsoon cloud clusters on 10 December 1978, *J. Atmos. Sci.*, 41(6), 933–960, doi:10.1175/1520-0469(1984)041<0933:DASOWM>2.0.CO;2.
- Del Genio, A. D., and W. Kovari (2002), Climatic properties of tropical precipitating convection under varying environmental conditions, *J. Clim.*, 15, 2597–2615, doi:10.1175/1520-0442(2002)015<2597:CPOTPC>2.0.CO;2.
- Dessler, A., and S. Sherwood (2000), Simulations of tropical upper tropospheric humidity, *J. Geophys. Res.*, 105(D15), 20,155–20,163, doi:10.1029/2000JD900231.
- Dong, X., B. Xi, and P. Minnis (2006), A climatology of midlatitude continental clouds from the ARM SGP Central Facility. Part II: Cloud fraction and surface radiative forcing, *J. Clim.*, 19(9), 1765–1783, doi:10.1175/JCLI3710.1.
- Dong, X., P. Minnis, B. Xi, S. Sun-Mack, and Y. Chen (2008), Comparison of CERES-MODIS stratus cloud properties with ground-based measurements at the DOE ARM Southern Great Plains site, *J. Geophys. Res.*, 113, D03204, doi:10.1029/2007JD008438.
- Feng, Z., X. Dong, and B. Xi (2009), A method to merge WSR-88D data with ARM SGP millimeter cloud radar data by studying deep convective systems, *J. Atmos. Oceanic Technol.*, 26(5), 958–971, doi:10.1175/2008JTECHA1190.1.
- Frederick, K., and C. Schumacher (2008), Anvil characteristics as seen by C-POL during the Tropical Warm Pool International Cloud Experiment (TWP-ICE), *Mon. Weather Rev.*, 136(1), 206–222, doi:10.1175/2007MWR2068.1.
- Futyant, J. M., and A. D. Del Genio (2007), Deep convective system evolution over Africa and the Tropical Atlantic, *J. Clim.*, 20(20), 5041–5060, doi:10.1175/JCLI4297.1.
- Hartmann, D. L., L. A. Moy, and Q. Fu (2001), Tropical convection and the energy balance at the top of the atmosphere, *J. Clim.*, 14(24), 4495–4511, doi:10.1175/1520-0442(2001)014<4495:TCAITEB>2.0.CO;2.
- Hong, Y., K. Hsu, S. Sorooshian, and X. Gao (2004), Precipitation estimation from remotely sensed imagery using an artificial neural network cloud classification system, *J. Appl. Meteorol.*, 43(12), 1834–1853, doi:10.1175/JAM2173.1.
- Houze, R. A., Jr. (1993), *Cloud Dynamics*, 573 pp., Academic, San Diego, Calif.
- Houze, R. A., Jr. (1997), Stratiform precipitation in regions of convection: A meteorological paradox?, *Bull. Am. Meteorol. Soc.*, 78(10), 2179–2196, doi:10.1175/1520-0477(1997)078<2179:SPIOC>2.0.CO;2.
- Houze, R. A., Jr. (2004), Mesoscale convective systems, *Rev. Geophys.*, 42, RG4003, doi:10.1029/2004RG000150.
- Houze, R. A., C. Cheng, C. A. Leary, and J. F. Gamache (1980), Diagnosis of cloud mass and heat fluxes from radar and synoptic data, *J. Atmos. Sci.*, 37(4), 754–773, doi:10.1175/1520-0469(1980)037<0754:DOCMHA>2.0.CO;2.
- Houze, R. A., Jr., M. I. Biggerstaff, S. A. Rutledge, and B. F. Smull, (1989), Interpretation of Doppler weather radar displays of midlatitude mesoscale convective systems, *Bull. Am. Meteorol. Soc.*, 70(6), 608–619, doi:10.1175/1520-0477(1989)070<0608:IODWRD>2.0.CO;2.
- Kennedy, A. D., X. Dong, B. Xi, P. Minnis, A. D. Del Genio, A. B. Wolf, and M. M. Khaiyer (2010), Evaluation of the NASA GISS single-column model simulated clouds using combined surface and satellite observations, *J. Clim.*, 23(19), 5175–5192, doi:10.1175/2010JCLI3353.1.
- Khaiyer, M. M., D. R. Doelling, P. K. Chan, M. L. Nordeen, R. Palikonda, and Y. Yi (2006), Derivation of improved surface and TOA broadband fluxes using CERES-derived narrowband-to-broadband coefficients, paper presented at AMS 12th Conference on Atmospheric Radiation, Am. Meteorol. Soc., Madison, Wisconsin.
- Khaiyer, M. M., P. Minnis, D. R. Doelling, R. Palikonda, M. Nordeen, Y. Yi, and D. Rutan (2011), Improved TOA shortwave and longwave broadband fluxes derived from the Southern Great Plains, paper presented at 2011 Atmospheric Science Research Science Team Meeting, U.S. Dep.

- of Energy, San Antonio, Texas, March 28–April 1. [Available at http://asr.science.energy.gov/meetings/stm/posters/poster_pdf/2011/P000311.pdf.]
- Kuligowski, R. J. (2002), A self-calibrating real-time GOES rainfall algorithm for short-term rainfall estimates, *J. Hydrometeorol.*, **3**(2), 112–130, doi:10.1175/1525-7541(2002)003<0112:ASCRTG>2.0.CO;2.
- Kummerow, C., et al. (2000), The status of the Tropical Rainfall Measuring Mission (TRMM) after two years in orbit, *J. Appl. Meteorol.*, **39**(12), 1965–1982, doi:10.1175/1520-0450(2001)040<1965:TSOTTR>2.0.CO;2.
- Kummerow, C., Y. Hong, W. S. Olson, S. Yang, R. F. Adler, J. McCollum, R. Ferraro, G. Petty, D. Shin, and T. T. Wilheit (2001), The evolution of the Goddard Profiling Algorithm (GPROF) for rainfall estimation from passive microwave sensors, *J. Appl. Meteorol.*, **40**(11), 1801–1820, doi:10.1175/1520-0450(2001)040<1801:TEOTGP>2.0.CO;2.
- Langston, C., J. Zhang, and K. Howard (2007), Four-dimensional dynamic radar mosaic, *J. Atmos. Oceanic Technol.*, **24**(5), 776–790, doi:10.1175/JTECH2001.1.
- Li, W., and C. Schumacher (2011), Thick anvils as viewed by the TRMM precipitation radar, *J. Clim.*, **24**(6), 1718–1735, doi:10.1175/2010JCLI3793.1.
- Lin, B., B. A. Wielicki, L. H. Chambers, Y. Hu, and K. Xu (2002), The Iris Hypothesis: A negative or positive cloud feedback?, *J. Clim.*, **15**(1), 3–7, doi:10.1175/1520-0442(2002)015<0003:TIHANO>2.0.CO;2.
- Lin, B., L. H. Chambers, K. Xu, T. Wong, B. A. Wielicki, and Y. Hu (2004), Examination of the decadal tropical mean ERBS nonscanner radiation data for the Iris Hypothesis, *J. Clim.*, **17**(6), 1239–1246, doi:10.1175/1520-0442(2004)017<1239:EOTDTM>2.0.CO;2.
- Lin, B., B. A. Wielicki, P. Minnis, L. Chambers, K.-M. Xu, Y. Hu, and A. Fan (2006), The effect of environmental conditions on tropical deep convective systems observed from the TRMM Satellite, *J. Clim.*, **19**(22), 5745–5761, doi:10.1175/JCLI3940.1.
- Lindzen, R. S., M. Chou, and A. Y. Hou (2001), Does the Earth have an adaptive infrared iris?, *Bull. Am. Meteorol. Soc.*, **82**(3), 417–432, doi:10.1175/1520-0477(2001)082<0417:DTEHAA>2.3.CO;2.
- Liou, K. (1986), Influence of cirrus clouds on weather and climate processes: A global perspective, *Mon. Weather Rev.*, **114**(6), 1167–1199, doi:10.1175/1520-0493(1986)114<1167:IOCCOW>2.0.CO;2.
- Machado, L. A. T., and W. B. Rossow (1993), Structural characteristics and radiative properties of tropical cloud clusters, *Mon. Weather Rev.*, **121**(12), 3234–3260, doi:10.1175/1520-0493(1993)121<3234:SCARPO>2.0.CO;2.
- Machado, L. A. T., W. B. Rossow, R. L. Guedes, and A. W. Walker (1998), Life cycle variations of mesoscale convective systems over the Americas, *Mon. Weather Rev.*, **126**(6), 1630–1654, doi:10.1175/1520-0493(1998)126<1630:LCVOMC>2.0.CO;2.
- Maddox, R. A. (1980), Mesoscale convective complexes, *Bull. Am. Meteorol. Soc.*, **61**(11), 1374–1387, doi:10.1175/1520-0477(1980)061<1374:MCC>2.0.CO;2.
- Melnikov, V. M., D. S. Zrnic, R. J. Doviak, P. B. Chilson, D. B. Mechem, and Y. L. Kogan (2011), Prospects of the WSR-88D radar for cloud studies, *J. Appl. Meteorol. Climatol.*, **50**(4), 859–872, doi:10.1175/2010JAMC2303.1.
- Miller, M. A., J. Verlinde, C. V. Gilbert, G. J. Lehenbauer, J. S. Tongue, and E. E. Clothiaux (1998), Detection of nonprecipitating clouds with the WSR-88D: A theoretical and experimental survey of capabilities and limitations, *Weather Forecast.*, **13**(4), 1046–1062, doi:10.1175/1520-0434(1998)013<1046:DONCWT>2.0.CO;2.
- Minnis, P., W. Smith, D. Garber, J. K. Ayers, and D. Doelling (1995), Cloud properties derived from GOES-7 for Spring 1994 ARM intensive observing period using version 1.0.0 of ARM Satellite Data Analysis Program, *NASA Ref. Publ.*, **1366**, 61 pp.
- Minnis, P., et al. (2008), Cloud detection in nonpolar regions for CERES using TRMM VIRS and Terra and Aqua MODIS data, *IEEE Trans. Geosci. Remote Sens.*, **46**(11), 3857–3884, doi:10.1109/TGRS.2008.2001351.
- Minnis, P., et al. (2011), CERES Edition-2 cloud property retrievals using TRMM VIRS and Terra and Aqua MODIS Data—Part I: Algorithms, *IEEE Trans. Geosci. Remote Sens.*, doi:10.1109/TGRS.2011.2144601, in press.
- Mullendore, G. L., A. J. Homann, K. Bevers, and C. Schumacher (2009), Radar reflectivity as a proxy for convective mass transport, *J. Geophys. Res.*, **114**, D16103, doi:10.1029/2008JD011431.
- Nesbitt, S. W., R. Cifelli, and S. A. Rutledge (2006), Storm morphology and rainfall characteristics of TRMM precipitation features, *Mon. Weather Rev.*, **134**(10), 2702–2721, doi:10.1175/MWR3200.1.
- Pandya, R. E., and D. R. Durran (1996), The influence of convectively generated thermal forcing on the mesoscale circulation around squall lines, *J. Atmos. Sci.*, **53**(20), 2924–2951, doi:10.1175/1520-0469(1996)053<2924:TIOCGT>2.0.CO;2.
- Ramanathan, V. (1987), The role of Earth radiation budget studies in climate and general circulation research, *J. Geophys. Res.*, **92**(D4), 4075–4095, doi:10.1029/JD092iD04p04075.
- Ramanathan, V., R. D. Cess, E. F. Harrison, P. Minnis, B. R. Barkstrom, E. Ahmad, and D. Hartmann (1989), Cloud-radiative forcing and climate: Results from the Earth Radiation Budget Experiment, *Science*, **243**(4887), 57–63, doi:10.1126/science.243.4887.57.
- Rickenbach, T. M. (1999), Cloud-top evolution of tropical oceanic squall lines from radar reflectivity and infrared satellite data, *Mon. Weather Rev.*, **127**(12), 2951–2976, doi:10.1175/1520-0493(1999)127<2951:CTEOTO>2.0.CO;2.
- Smith, W. L., P. Minnis, H. Finney, R. Palikonda, and M. M. Khaiyer (2008), An evaluation of operational GOES-derived single-layer cloud top heights with ARSCL data over the ARM Southern Great Plains Site, *Geophys. Res. Lett.*, **35**, L13820, doi:10.1029/2008GL034275.
- Soden, B. J. (2000), The diurnal cycle of convection, clouds, and water vapor in the tropical upper troposphere, *Geophys. Res. Lett.*, **27**(15), 2173–2176, doi:10.1029/2000GL011436.
- Soden, B. J., D. D. Turner, B. M. Lesht, and L. M. Miloshevich (2004), An analysis of satellite, radiosonde, and lidar observations of upper tropospheric water vapor from the Atmospheric Radiation Measurement Program, *J. Geophys. Res.*, **109**, D04105, doi:10.1029/2003JD003828.
- Steiner, M., R. A. Houze, and S. E. Yuter (1995), Climatological characterization of three-dimensional storm structure from operational radar and rain gauge data, *J. Appl. Meteorol.*, **34**, 1978–2007, doi:10.1175/1520-0450(1995)034<1978:CCOTDS>2.0.CO;2.
- Stephens, G. L. (2005), Cloud feedbacks in the climate system: A critical review, *J. Clim.*, **18**, 237–273, doi:10.1175/JCLI3243.1.
- Vicente, G. A., R. A. Scofield, and W. P. Menzel (1998), The operational GOES infrared rainfall estimation technique, *Bull. Am. Meteorol. Soc.*, **79**(9), 1883–1898, doi:10.1175/1520-0477(1998)079<1883:TOGIRE>2.0.CO;2.
- Webster, P. J., and G. L. Stephens (1980), Tropical upper-tropospheric extended clouds: Inferences from winter MONEX, *J. Atmos. Sci.*, **37**(7), 1521–1541, doi:10.1175/1520-0469-37.7.1521.
- Xi, B., X. Dong, P. Minnis, and M. M. Khaiyer (2010), A 10 year climatology of cloud fraction and vertical distribution derived from both surface and GOES observations over the DOE ARM SPG site, *J. Geophys. Res.*, **115**, D12124, doi:10.1029/2009JD012800.
- Yang, P., L. Zhang, G. Hong, S. L. Nasiri, B. A. Baum H.-L. Huang, M. D. King, and S. Platnick (2007), Differences between collection 4 and 5 MODIS ice cloud optical/microphysical products and their impact on radiative forcing simulations, *IEEE Trans. Geosci. Remote Sens.*, **45**(9), 2886–2899.
- Yuan, J., and R. A. Houze (2010), Global variability of mesoscale convective system anvil structure from A-Train satellite data, *J. Clim.*, **23**, 5864–5888, doi:10.1175/2010JCLI3671.1.
- Yuter, S. E., and R. A. Houze (1998), The natural variability of precipitating clouds over the western Pacific warm pool, *Q. J. R. Meteorol. Soc.*, **124**, 53–99, doi:10.1002/qj.49712454504.
- Zeng, X., W.-K. Tao, M. Zhang, A. Y. Hou, S. Xie, S. Lang, X. Li, D. Starr, X. Li, and J. Simpson (2009a), An indirect effect of ice nuclei on atmospheric radiation, *J. Atmos. Sci.*, **66**, 41–61, doi:10.1175/2008JAS2778.1.
- Zeng, X., J. Simpson, W.-K. Tao, M. Zhang, A. Y. Hou, S. Xie, S. Lang, X. Li, D. O. Starr, and X. Li (2009b), A contribution by ice nuclei to global warming, *Q. J. R. Meteorol. Soc.*, **135**, 1614–1629, doi:10.1002/qj.449.
- Zhang, J., K. Howard, and J. J. Gourley (2005), Constructing three-dimensional multiple-radar reflectivity mosaics: Examples of convective storms and stratiform rain echoes, *J. Atmos. Oceanic Technol.*, **22**, 30–42, doi:10.1175/JTECH-1689.1.
- Zhang, J., K. Howard, and S. Wang (2006), Single radar Cartesian grid and adaptive radar mosaic system, paper presented at 12th Conference on Aviation, Range, and Aerospace Meteorology, Am. Meteorol. Soc., Atlanta, Ga.
- Zhang, J., et al. (2011), National Mosaic and Multi-Sensor QPE (NMQ) system: Description, results, and future plans, *Bull. Am. Meteorol. Soc.*, **92**(10), 1321–1338, doi:10.1175/2011BAMS-D-11-0047.1.
- Zhang, Y., and S. A. Klein (2010), Mechanisms affecting the transition from shallow to deep convection over land: Inferences from observations of the diurnal cycle collected at the ARM Southern Great Plains site, *J. Atmos. Sci.*, **67**, 2943–2959, doi:10.1175/2010JAS3366.1.

X. Dong, Z. Feng, and B. Xi, Department of Atmospheric Sciences, University of North Dakota, 4149 University Ave., Box 9006, Grand Forks, ND 58202-9006, USA. (dong@aero.und.edu)

M. Khaiyer and P. Minnis, NASA Langley Research Center, Hampton, VA 23681-2199, USA.

C. Schumacher, Department of Atmospheric Sciences, Texas A&M University, College Station, TX 77843, USA.